Nanoscale Advances

ROYAL SOCIETY OF CHEMISTRY

PAPER

View Article Online
View Journal | View Issue

Check for updates

Cite this: *Nanoscale Adv.*, 2022, **4**, 211

MoS_2/cellulose-doped ZnO nanorods for catalytic, antibacterial and molecular docking studies†

Muhammad Ikram, *[a] Muhammad Imran,[b] Shoukat Hayat,[c] Anum Shahzadi,[d] Ali Haider,[e] Sadia Naz,[f] Anwar Ul-Hamid, *[g] Walid Nabgan, *[h] Iqra Fazal[c] and Salamat Ali[c]

Cellulose nanocrystals (CNCs) and molybdenum disulphide (MoS_2) incorporated into ZnO nanorods (NRs) were synthesized *via* a chemical precipitation route at room temperature. All concerned samples were characterized to examine their optical properties, elemental composition, phase formation, surface morphology and functional group presence. The aim of this research was to enhance the catalytic properties of ZnO by co-doping with various concentrations of CNCs and MoS_2 NRs. It was renowned that doped ZnO NRs showed superior catalytic activity compared to bare ZnO NRs. Statistically significant ($p < 0.05$) inhibition zones for samples were recorded for *E. coli* and *S. aureus* at low and high concentrations, respectively. The *in vitro* bactericidal potential of ZnO-CNC and ZnO-CNC-MoS_2 nanocomposites was further confirmed through *in silico* molecular docking predictions against the DHFR and DHPS enzymes of *E. coli* and *S. aureus*. Molecular docking studies suggested the inhibition of these enzyme targets by CNC nanocomposites as a possible mechanism governing their bactericidal activity.

Received 24th August 2021
Accepted 30th October 2021

DOI: 10.1039/d1na00648g

rsc.li/nanoscale-advances

Open Access Article. Published on 01 November 2021. Downloaded on 4/23/2026 6:19:45 PM.
This article is licensed under a Creative Commons Attribution-NonCommercial 3.0 Unported Licence.

1. Introduction

Today's technology driven society with a plethora of economic activities has resulted in rapidly increasing aquatic pollution that has emerged as a big challenge to scientists and researchers all over the world.[1,2] Moreover, the unwavering growth of multiple industries including textile, chemical, plastic and paper sectors releases toxic dyes into water bodies that can contaminate the whole environment and cause harm to plants, animals, and humans.[1] Diseases that afflict humanity including hepatitis, diarrhoea, cryptosporidiosis, encephalitis and leptospirosis as well as typhoid fever spread worldwide due to polluted water. Globally, the reported cases for hepatitis A stand at 1.4 million diagnosed annually with a mortality count of about 12 800 to 16 100.[3] Hazardous pollutants present in wastewater include both inorganic as well as organic heavy metals, harmful solvents and compounds, which need to be essentially decomposed to achieve a sustainable green environment.[4] Hence, pollutant removal from water has garnered much attention due to their alarming effects on human health and the environment.

Multiple methods have been reported for removing contaminants such as dyes from industrial discharges including a membrane separation process,[5] coagulation,[6] adsorption,[7] photo-oxidation,[8] an electrochemical process,[9] an advanced oxidation process[10] and chemical oxidation.[11] Among all, photocatalysis based on a metal oxide semiconductor has gained the utmost attention for wastewater treatment.[11] Recently, metal oxides (MOs) such as SnO_2, MnO_2, TiO_2, MgO, CeO_2, Fe_2O_3 and CaO_2 were used as the prime choice for photocatalysis due to their low cost, chemical inertness, chemical stability and nontoxicity, which make them effective for various applications such as water purification, hydrogen generation and sterilization.[4,12] Among all MOs, ZnO (n-type semiconductor) has received the most attention due to greater surface reactivity, excellent photosensitivity, low price and more importantly being friendly to the environment.[13–15] Upon

[a]*Solar Cell Application Research Lab, Department of Physics, Government College University Lahore, Lahore, 54000, Punjab, Pakistan. E-mail: dr.muhammadikram@gcu.edu.pk*

[b]*State Key Laboratory of Chemical Resource Engineering, Beijing Advanced Innovation Centre for Soft Matter Science and Engineering, Beijing Engineering Center for Hierarchical Catalysts, Beijing University of Chemical Technology, Beijing 100029, China*

[c]*Department of Physics, Riphah Institute of Computing and Applied Sciences (RICAS), Riphah International University, 14 Ali Road, Lahore, Pakistan*

[d]*Faculty of Pharmacy, University of the Lahore, Lahore, Pakistan*

[e]*Department of Clinical Medicine and Surgery, University of Veterinary and Animal Sciences, Lahore 54000, Punjab, Pakistan*

[f]*Tianjin Institute of Industrial Biotechnology, Chinese Academy of Sciences, Tianjin 300308, China*

[g]*Core Research Facilities, King Fahd University of Petroleum & Minerals, Dhahran, 31261, Saudi Arabia. E-mail: anwar@kfupm.edu.sa*

[h]*School of Chemical and Energy Engineering, Faculty of Engineering, Universiti Teknologi Malaysia, 81310 Skudai, Johor, Malaysia. E-mail: wnabgan@gmail.com*

† Electronic supplementary information (ESI) available. See DOI: 10.1039/d1na00648g

© 2022 The Author(s). Published by the Royal Society of Chemistry

Open Access Article. Published on 01 November 2021. Downloaded on 4/23/2026 6:19:45 PM.
This article is licensed under a Creative Commons Attribution-NonCommercial 3.0 Unported Licence.

exposing ZnO nanoparticles to UV light, the generation of hydroxyl radicals takes place. They are considered strong candidates for the oxidation process, which serves to degrade dye and organic contaminants present in wastewater. However, there could be some difficulties such as lower stability that might be attributed to the photo-corrosion phenomenon during light fall and stretched bandgap energy that permits mineralization under UV light.[13,16] Many ways are adopted to enhance the photocatalytic efficiency of ZnO through linking with an n-type semiconductor with suitable materials such as carbon materials, noble metals and lower bandgap semiconductors.

Recently, molybdenum disulphide (MoS_2), which has a structure similar to graphene containing S–Mo–S layers joined by van der Waals forces, appeared as one of the promising materials employed for photocatalysis. It exhibits chemical inertness, high conductivity and unique optical properties, which make it an ideal substance for a variety of applications (*e.g.*, catalysis, phototransistors, and sensing).[13,17] Due to these properties, its semiconductor coupling can be undertaken with materials such as ZnO to produce heterojunctions that possibly can enhance photocatalytic effectiveness.[1] Cellulose (CNC) is one of the utmost utilized, naturally decomposable and renewable natural polysaccharide materials, frequently employed for polymer synthesis and as a stabilizing agent due to the abundance of hydroxyl groups that enable it to act as a stabilizing agent.[11,18] These hydroxyl groups in the CNC structure interact efficiently with metal ions, while inorganic NPs disperse uniformly on the CNC matrix and as a result improve metal NP reaction capability. Moreover, employing CNC as a substrate is promising for catalyst recovery, which exhibits high adsorption capability and boosts the process of catalytic degradation of pollutants.[19]

In this work, ZnO, CNC, and ZnO-CNC with various concentrations of MoS_2 (50 and 100 mg)-doped ZnO were synthesised successfully. The optical properties, structures and morphologies of all relevant samples were studied. This research aims to evaluate the influence of co-dopant (CNC/MoS_2) concentration on the catalytic and antibacterial activity of MoS_2/CNC-doped ZnO. Furthermore, molecular docking predictions of CNC-ZnO and MoS_2/CNC-doped ZnO nanocomposites against the DHFR and DHPS enzymes of the folate biosynthetic pathway were performed to unveil their role as antibacterial agents.

2. Methods

The current study was aimed to synthesize MoS_2 doped into a fixed amount of cellulose-doped ZnO nanorods through a co-precipitation route to investigate the catalytic activity and the efficacy of the antibacterial agent against antibiotic-resistant bacteria with molecular docking.

2.1 Materials and reagents

Sodium hydroxide (NaOH, 98%), zinc nitrate hexahydrate ($Zn(NO_3)_2 \cdot 6H_2O$, 99%), molybdenum disulphide (MoS_2, 99.8%), microcrystalline cellulose ($C_6H_{10}O_5$, 99.5%) and sulfuric acid (H_2SO_4) were acquired from Sigma Aldrich and Analar (USA).

2.2 Synthesis of cellulose nanocrystals

Using the hydrolysis method, avicel (10 g) was incorporated into H_2SO_4 and deionized water (DI water) solution (50%), to synthesize cellulose. Under continuous stirring, the solution was heated for 45 minutes at 70 °C. Afterwards in yellow brownish solution, 5000 mL of DI water was added to dilute H_2SO_4 and centrifuged at 7100 rpm for 6 minutes. The cycles of washing/centrifugation were repeated until the pH of the solution approached neutral using NaOH. The resulting solution was heated at 100 °C to acquire the solid content of cellulose nanocrystals (CNCs) (Fig. 1(a)).[20,21]

2.3 Synthesis of MoS_2/cellulose-doped ZnO NRs

In the current work, undoped ZnO and MoS_2/CNC-doped ZnO NRs were prepared *via* a simple co-precipitation technique using $Zn(NO_3) \cdot 4H_2O$, deionized water, NaOH and MoS_2. Firstly, $Zn(NO_3)_2 \cdot 4H_2O$ (0.5 M) was dissolved in a 100 mL deionized water (DI water) under constant stirring to get the zincates. After that a fixed amount (2.5 mL) of as-prepared CNC was incorporated into the zincate solution. Secondly, different concentrations (50 and 100 mg) of MoS_2 were added into the solution mixture and stirred continuously. Aqueous solution containing (0.5 M) NaOH was used to maintain the pH of zincate solution up to 12 under continuous stirring for 30 minutes at 80 °C. The zincate precipitate was separated *via* a centrifuge machine at 7100 rpm for 6 minutes, heated at 85 °C for 20 hours (h), and ground using a mortar and pestle to acquire fine powder. In the absence of doping products (CNC and MoS_2), a similar procedure was adopted to synthesize pristine ZnO NRs (Fig. 1(b)).[22] Following samples (ZnO, CNC, CNC-doped ZnO and various different concentrations (50 and 100 mg) of MoS_2 doped in ZnO-CNC named as ZCM1 and ZCM2 were prepared.

2.4 Isolation and characterization of bacteria

Lactating Caprine mastitic fluid was obtained from farms and several private clinics across Punjab, Pakistan, and cultured on 5% blood agar. After 24 hours of incubation at 37 °C,[23] the derived colonies were flicked in triplicates on Mannitol salt agar (MSA) and MacConkey agar (MA) to harvest pure *Escherichia coli* (*E. coli*) and *Staphylococcus aureus* (*S. aureus*) isolates. Refined colonies were verified by Gram staining for morphological assessment and biochemical testing (*i.e.* catalase and coagulase).[24]

2.5 Antibacterial activity

All samples were investigated for antimicrobial activities using the agar well diffusion method by swabbing 1.5 10^8 CFU mL^{-1} of *S. aureus* and *E. coli* on MA and MSA, respectively. Bacterial cultures were swabbed onto agar plates, and wells of 6 mm diameter were created using a sanitized borer.[23,24] Distinct amounts of ZnO, CNC, and MoS_2/CNC-doped ZnO (0.5 and 1.0 mg/50 μL) were loaded into each well and sorted with

© 2022 The Author(s). Published by the Royal Society of Chemistry

Open Access Article. Published on 01 November 2021. Downloaded on 4/23/2026 6:19:45 PM.
This article is licensed under a Creative Commons Attribution-NonCommercial 3.0 Unported Licence.

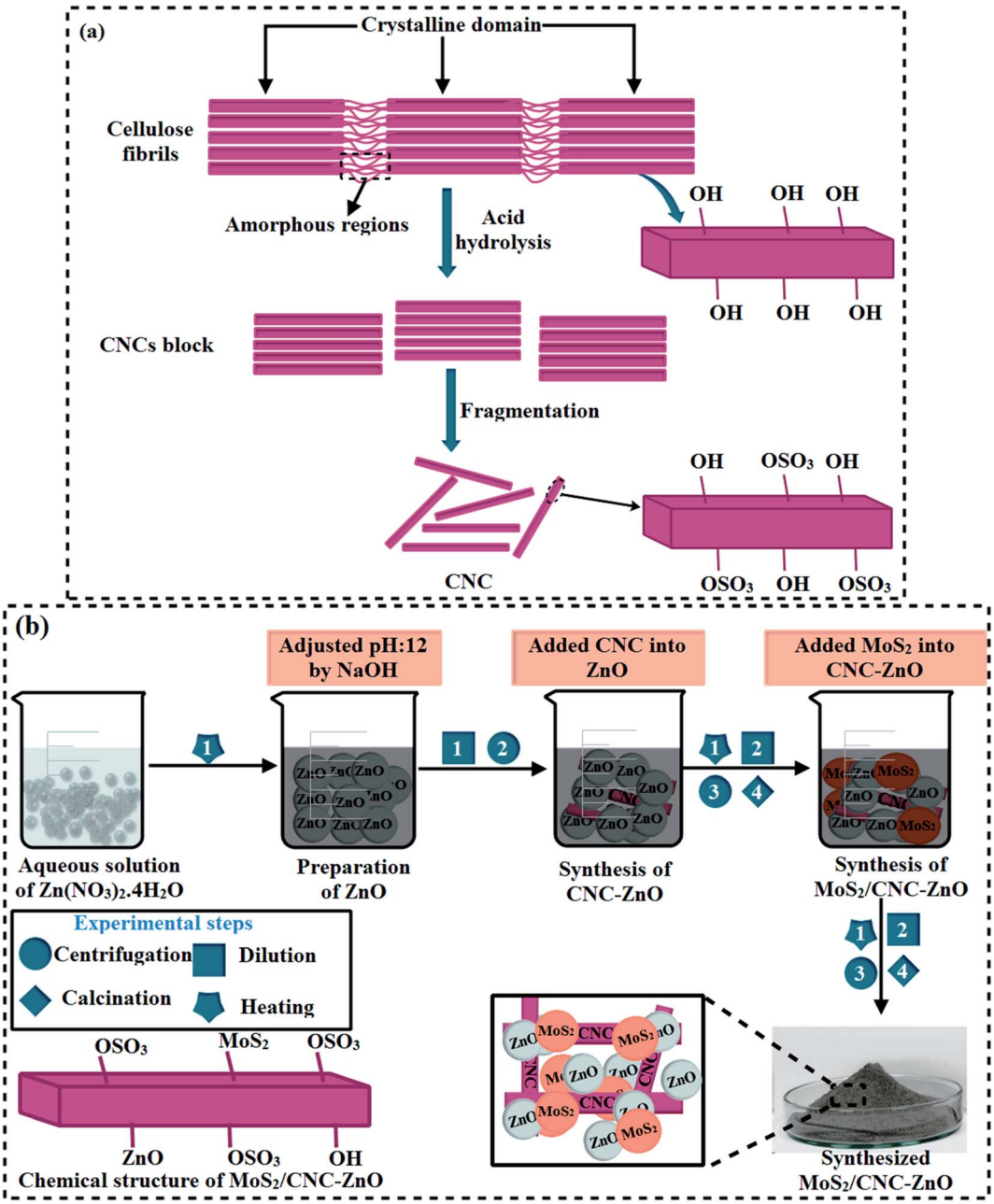

Fig. 1 (a) Sulfate groups present on the surface of cellulose are depicted in a schematic diagram. (b) Schematic presentation of the preparation and structure of MoS_2/CNC-doped ZnO NTs.

Ciprofloxacin (0.005 mg/50 μL) and DI water (50 μL) as positive (+ve) and negative (−ve) standards, respectively. Antibacterial efficacy was determined by monitoring inhibitory zones in millimetres (mm) using a Vernier calliper after 24 hours of incubation of filled agar plates at 37 °C. A one-way variance analysis (ANOVA) was adapted to determine the antibacterial viability of the synthesised materials.[24,25]

2.6 Molecular docking studies

Molecular docking studies were employed to rationalize the mechanism governing the bactericidal activity of ZnO-CNC and ZnO-CNC-MoS_2 nanocomposites. Recently, the role of metal-doped CNC nanocomposites as bactericidal agents has been reported. Identifying interactions responsible for their inhibition potency against essential enzyme targets is worthy of further exploration.[26] Here, we performed molecular docking studies of these nanocomposite systems against DHFR and DHPS enzymes belonging to the folate biosynthetic pathway of *E. coli* and *S. aureus* to unveil the mystery behind their biocidal potential.

The crystal structure of enzymes were retrieved from the protein data bank with the accession code 2ANQ (Resolution: 2.13 Å)[27] for $DHFR_{E.\ coli}$, 5U0W (Resolution: 1.97 Å) for $DHPS_{E.}$

© 2022 The Author(s). Published by the Royal Society of Chemistry

Open Access Article. Published on 01 November 2021. Downloaded on 4/23/2026 6:19:45 PM.
This article is licensed under a Creative Commons Attribution-NonCommercial 3.0 Unported Licence.

coli,[28] and 4FGG (resolution: 2.30 Å) for $DHFR_{S.\ aureus}$.[29] The selected enzyme structures were prepared for docking predictions using the method reported in our previous studies.[30,31] Docking predictions were performed using ICM Molsoft software,[32] where basic steps involved the removal of the native ligand and water of crystallization followed by the addition of polar H atoms and energy minimization. The active pocket was defined within 10 Å of the co-crystalized ligand to specify the docking position of nanocomposites in the current study. The monomeric structure of ZnO-CNC and ZnO-CNC-MoS_2 was prepared using the ligedit tool of ICM and top ranked docking conformations were selected for further analysis using Pymol software and ICM Molsoft visualizer.

2.7 Catalytic activity

The catalytic activity of ZnO and co-doped ZnO NRs was evaluated against methylene blue (MB) dye in the solution with a specific quantity of $NaBH_4$ (400 μL and 800 μL). In the present study, a quartz cell was filled with 400 μL solution of $NaBH_4$ and 3 mL aqueous methylene blue. Upon addition of NRs into the solution containing $NaBH_4$ and MB, dye degradation was observed as depicted in Fig. 2.[20] In order to acquire absorption spectra at different intervals, UV-vis spectroscopy was employed at wavelengths ranging from 200 to 700 nm.

2.8 Characterization of samples

The structure and crystalline behavior of the produced powders were determined with XRD using a powder diffractometer (PAN Analytical X′ pert PRO type X-ray diffractometer) and monochromatic Cu-K_α radiation (λ = 1.5418 Å) at a scan rate of 5° min^{-1} in the 2θ° range of 5° to 80°. On an Excalibur 3100 spectrometer, FTIR spectroscopy was carried out within a spectral range of 4000–400 cm^{-1}. A scanning electron microscope (SEM), JEOL JSM-6460LV and JEOL JEM-2100F high-resolution transmission electron microscopes (HR-TEM) were used to analyze the morphology, particle size and interlayer spacing. Using a UV-vis spectrophotometer (Genesys 10S) in the range of 180–400 nm, optical properties were investigated. Raman spectra with a laser wavelength of 532 nm (6 mW) were recorded with a Renishaw through a reflex confocal Raman microscope. The spectra of photoluminescence (PL) were recorded with a spectrofluorometer for the as-prepared and doped samples (JASCO, FP-8300).

3. Results and discussion

As shown in Fig. 3(a), XRD was conducted to acquire information about the crystal structure and phase constitution and calculate the crystallite size of ZnO nanorods (NRs), ZnO-CNC, (0.1) MoS_2@CNC/ZnO (ZCM1) and (0.2) MoS_2@CNC/ZnO (ZCM2). The pristine ZnO NRs exhibited peaks at 2θ° of 31.68°, 34.44°, 36.24°, 47.66°, 56.62°, 62.98° and 67.99°, which are compatible with (100), (002), (101), (102), (110), (103) and (112) crystal planes, respectively. These planes are well synchronized with JCPDS no. 36-1451 and confirm the formation of a hexagonal wurtzite structure.[33] ZnO crystal formation with an oriented (101) lattice plane is responsible for the

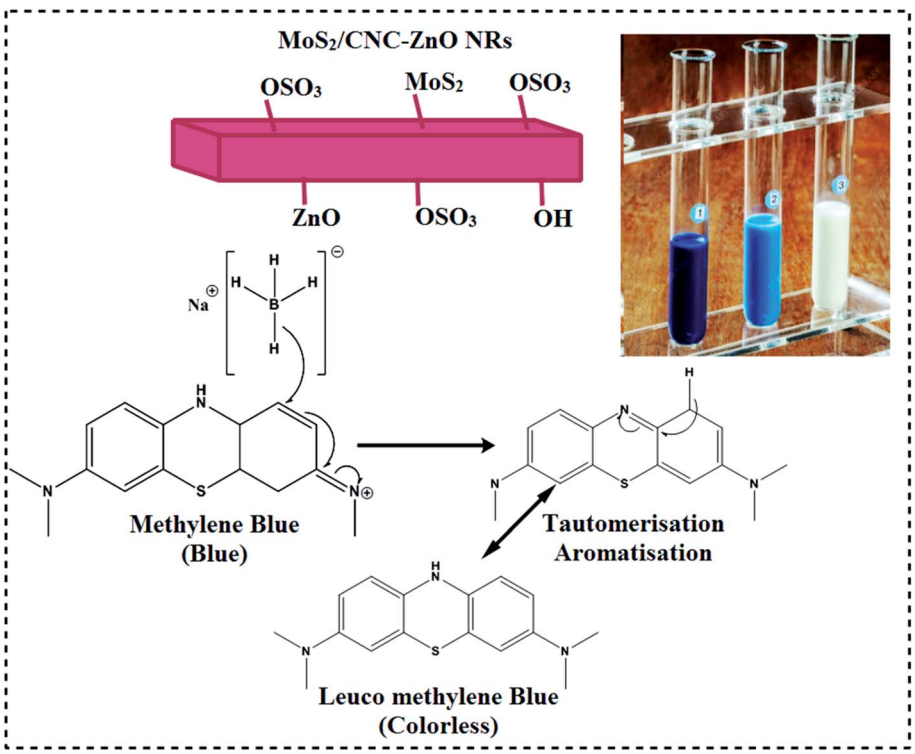

Fig. 2 Catalysis mechanisms of the prepared samples.

© 2022 The Author(s). Published by the Royal Society of Chemistry

Open Access Article. Published on 01 November 2021. Downloaded on 4/23/2026 6:19:45 PM.
This article is licensed under a Creative Commons Attribution-NonCommercial 3.0 Unported Licence.

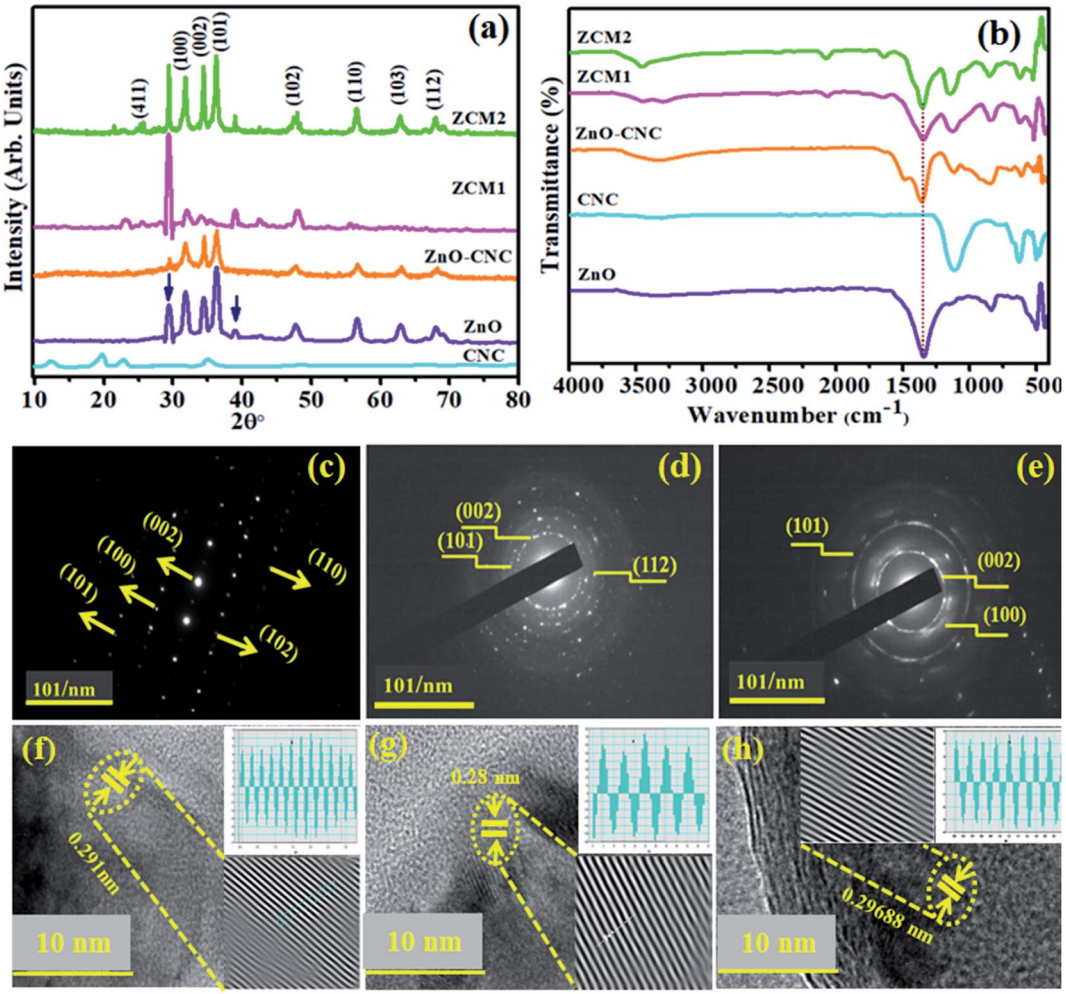

Fig. 3 (a) XRD patterns, (b) FTIR spectra (c–e), and SAED patterns of ZnO, CNC and ZCM_2 and (f–h) *d*-spacing images of ZnO and co-doped ZnO NRs.

highest peak at $2\theta^\circ = 36.24^\circ$. For the CNC plane, diffraction peaks at 13°, 19.5°, 22.4° and 34° are indexed to (101), (101), (002) and (112) planes revealing its monoclinic structure (JCPDS card no. 46-0905).[34] It can be seen that upon CNC doping in ZnO, no cellulose peak was detected in the XRD pattern. Two additional peaks for all prepared samples flexing at $2\theta^\circ = 29.4^\circ$ and 39.04° represent the impurities of the zinc carboxyl-containing compound (marked by a blue arrow). These zinc traces could have formed as a result of the Zn precursor reacting with other reactants during the synthesis process.[35,36] The peaks emerging at 26.2° and ascribed to the (411) plane of hexagonal MoS_2 well matched with JCPDS card no. (37-1492).[25] We also found that in MoS_2 doped patterns, the intensity of diffraction peaks increased, which suggested an improved crystalline quality upon increasing the concentration of MoS_2. The crystallite sizes of NRs were calculated from the XRD pattern using the Scherrer formula. The computed crystallite sizes are 26.2, 10.17, 23.9, 42.6 and 48.5 for ZnO, CNC, ZnO-CNC, ZCM1 and ZCM2, respectively. As can be seen upon doping of CNC into ZnO the crystallite size decreased, which might be due to the replacement of the CNC element for the ZnO element, while upon incorporation of MoS_2 into ZnO, the crystallite size increased. Furthermore, FTIR spectroscopy was conducted for the identification of possible functional groups present on the synthesised samples and corresponding results are shown in Fig. 3(b).The absorption peak located at ~3369 cm^{-1} ascribed to the stretching vibration of OH was influenced by the moisture content in air.[11,37] The band at ~829 cm^{-1} represents the ZnO lattice vibrational frequency, while the peaks flexing at 1329 cm^{-1} and 669 cm^{-1} were attributed to ZnO formation.[13,38] The CNC absorption peak observed at 1110 cm^{-1} derived from C–O–C pyranose ring vibration.[39] More importantly upon MoS_2 doping, two additional peaks at 1638 cm^{-1} and 2069 cm^{-1} were observed, which might be linked with the Mo–S vibration. The vibration of spectra and the change in peak intensity again provide evidence for the substitution of MoS_2/CNC into ZnO, successfully. Subsequently, the selected area electron diffraction (SAED) ring patterns of undoped and doped NRs exhibited distinct bright spots as shown in Fig. 3(c–e). The observed rings provided strong evidence for the fact that products were highly

Open Access Article. Published on 01 November 2021. Downloaded on 4/23/2026 6:19:45 PM.
This article is licensed under a Creative Commons Attribution-NonCommercial 3.0 Unported Licence.

crystalline while ring indexing matched with XRD patterns nicely. The interlayered spacing (*d*-spacing) of all prepared nanocomposites was measured using HR-TEM (10 nm) images as shown in Fig. 3(f–h). *d*-Spacing values for ZnO, CNC and ZCM2 were calculated to be 0.291, 0.281 and 0.296 nm, respectively. The calculated *d*-spacing values correlated well with the XRD patterns.

The optical properties of the concerned materials were analyzed through UV-vis spectroscopy in the 200–800 nm range. The absorption spectra of pristine ZnO and CNC with different concentrations of MoS_2 (50 and 100 mg) are depicted in Fig. 4(a). All prepared samples showed maximum absorption in the range 250–400 nm. The maximum absorption peak of ZnO NRs was found at 375 nm,[40] and a clear blueshift for ZnO-CNC, ZCM1 and ZCM2 samples was noticed as compared to pristine. The observed blueshift indicated a change in the band structure of host ZnO NRs. The energy band gap (E_g) was calculated using Tauc's equation; graphs were plotted for $(\alpha h\nu)^2$ *vs.* $(h\nu)$ and the corresponding results are depicted in Fig. 4(b). E_g was calculated to be 3.2, 3.3, 3.1, 2.4 and 2.3 eV for CNC, ZnO, ZnO-CNC and MoS_2/CNC-doped ZnO, respectively. The addition of two types of impurity elements caused lattice strain in the structure of the crystal, which might be a consequence of variation in the energy band structure of doped samples.[41,42]

The Raman spectra of ZnO, CNC, ZnO-CNC, ZCM1 and ZCM2 were recorded at room temperature and are depicted in Fig. 4(d). The characteristic band of ZnO found at 1179 cm^{-1} was assigned to the scattering process of the ZnO wurtzite structure.[11,43] a strong band centered at ~1005 cm^{-1} and a weak band from ~1167 to 1194 cm^{-1} were observed, which confirmed the presence of CNC in the mapped area. A clear blueshift in Raman spectra for ZnO-CNC, ZCM1 and ZCM2 was observed, as shown in Fig. 4(d). It indicated that upon doping of MoS_2 into the ZnO matrix, the original wurtzite structure of pristine was changed due to introduced vacancies, substitution defects and reduced crystal symmetry.[44] Bands at 964 and 1066 cm^{-1} were found in the spectra of ZnO-CNC, ZCM1 and ZCM2 composites as compared to bare ZnO, suggesting that CNC and MoS_2 were successfully loaded on the ZnO surface.

Photoluminescence spectroscopy (PL) was employed to further examine the transfer behaviour of electron–hole pairs (e^- – h^+) and the rate of recombination and trapping in semiconductors.[13,45] A low PL intensity indicates a lower e^- –

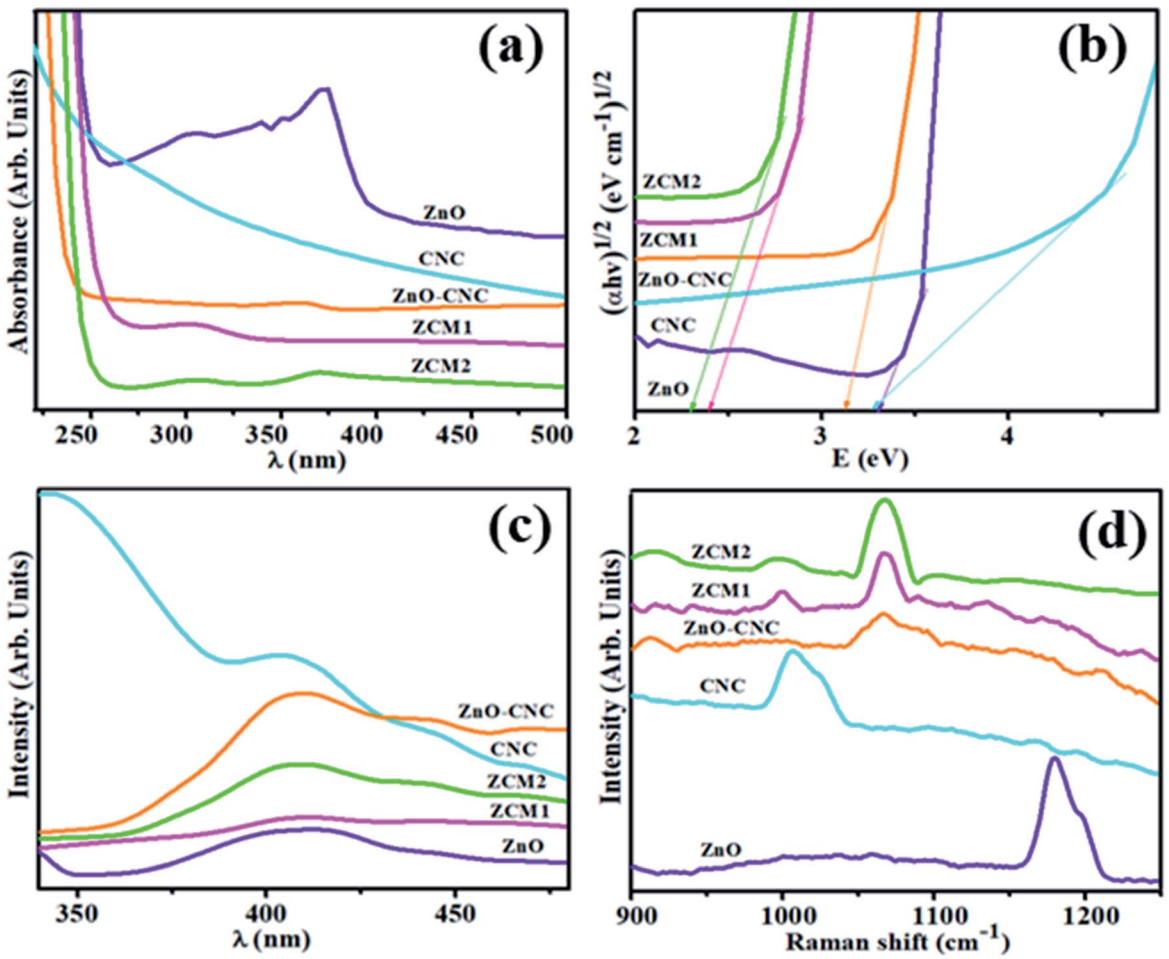

Fig. 4 (a) Uv-Vis spectra, (b) Tauc plots for the band gap, (c) photoluminescence spectra (PL) and (d) Raman spectra of undoped and doped ZnO NRs.

© 2022 The Author(s). Published by the Royal Society of Chemistry

Open Access Article. Published on 01 November 2021. Downloaded on 4/23/2026 6:19:45 PM.
This article is licensed under a Creative Commons Attribution-NonCommercial 3.0 Unported Licence.

h^+ recombination rate under light irradiation. On the other hand, a high PL intensity manifests a higher e^- – h^+ recombination rate, which is detrimental to photocatalytic activity. The PL spectra of ZnO, CNC, ZnO-CNC, ZCM1 and ZCM2 were recorded at room temperature and the corresponding results are shown in Fig. 4(c). For pristine ZnO, the shallow donor level of oxygen vacancies in the valence band (VB) corresponds to the blue emission peak at a 408 nm wavelength.[13] The PL spectra of CNC with the peak position at 410 nm could originate from carbonyl groups and various types of low-molecular derivatives of CNC destruction.[46] Upon loading of MoS_2 into ZnO, the PL intensity was suppressed for the sample ZCM1, suggesting that the e^- – h^+ rate was reduced, which increases the ability of electron immigration. However, the peak intensity in the sample ZCM2 once again increased upon increasing the concentration of MoS_2, which indicated that further doping of MoS_2 into ZnO was not suitable for the photocatalyst.[47]

In order to acquire information regarding the surface elemental composition of pristine ZnO NRs, CNC, ZnO-CNC, ZCM1 and ZCM2 EDS analysis was performed. The formation of ZnO NRs was confirmed by the presence of Zn and O peaks as shown in Fig. 5(a), while the peaks of C, Mo and S in ZCM1 and ZCM2 samples demonstrated the successful loading of CNC and MoS_2 atoms into the lattice. A peak of sodium (Na) was observed for the synthesized samples, which emanate from NaOH used to retain the pH of the samples. Furthermore, the additional elements in Fig. 4(b–e) Ca, Cu and Si might be due to the sample holder, conductive tape or some contamination.

HR-TEM was carried out to confirm the morphology of ZnO and MoS_2/CNC-doped ZnO NRs. Fig. 6 (a and inset) reveals nanorods of ZnO synthesized *via* a one pot co-precipitation route, while Fig. 6b shows a nanocluster of CNC. The addition of CNC to NRs causes the agglomeration of nanoclusters with a small size (Fig. 6c). MoS_2/CNC dopants agglomerated on NRs; increasing the quantity of dopants on NRs resulted in increased agglomeration, implying a random distribution of CNC and MoS_2 with NRs Fig. 6(d–e).

XPS analysis was used to understand the development of additional MoS_2/CNC-doped ZnO NRs. The surface content and valence states of the produced NRs are shown in Fig. 7(a, b). XPS analysis indicates the origin of component elements with a favourable reaction. The high-resolution spectrum of Mo 3d in Fig. 7(a) shows two binding energy levels, 229.1 and 232.1 eV for Mo $3d_{5/2}$ and Mo $3d_{3/2}$, respectively, confirming the heterostructure's Mo(IV) state.[48] Mo $3d_{5/2}$ and Mo $3d_{3/2}$ binding energies show that the Mo ions in the produced material are in distinct oxidative states.[49] The Zn 2p peaks in Fig. 7(b) are the typical peaks of the Zn2+ oxidation state in ZnO at 1021.4 eV and 1044.4 eV, which correspond to comparable Zn $2p_{3/2}$ and Zn $2p_{1/2}$ values in pure ZnO, respectively.[50]

The *in vitro* antibacterial effectiveness of pristine ZnO and MoS_2/CNC-doped ZnO NRs was assessed by measuring inhibition zones (mm) *via* an agar-based diffusion technique against *E. coli* and *S. aureus* and the corresponding results are

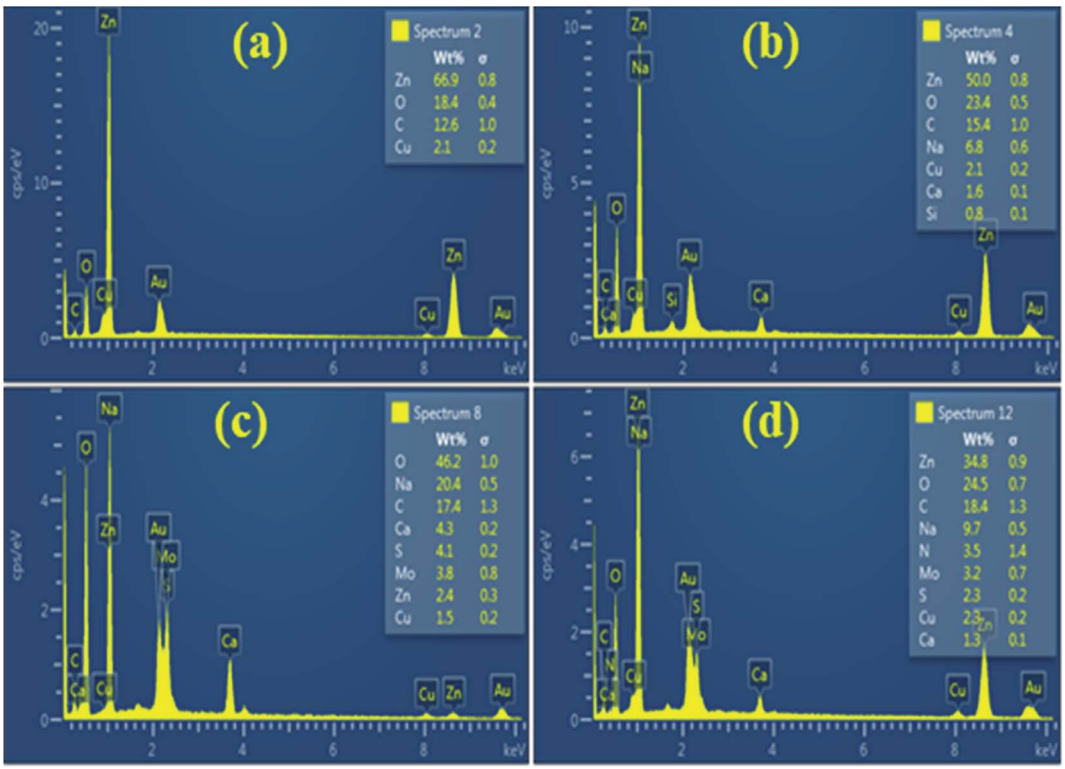

Fig. 5 EDS spectra of ZnO and co-doped ZnO NRs (a–d) with the MoS_2 content (50 and 100 mg).

Open Access Article. Published on 01 November 2021. Downloaded on 4/23/2026 6:19:45 PM.
This article is licensed under a Creative Commons Attribution-NonCommercial 3.0 Unported Licence.

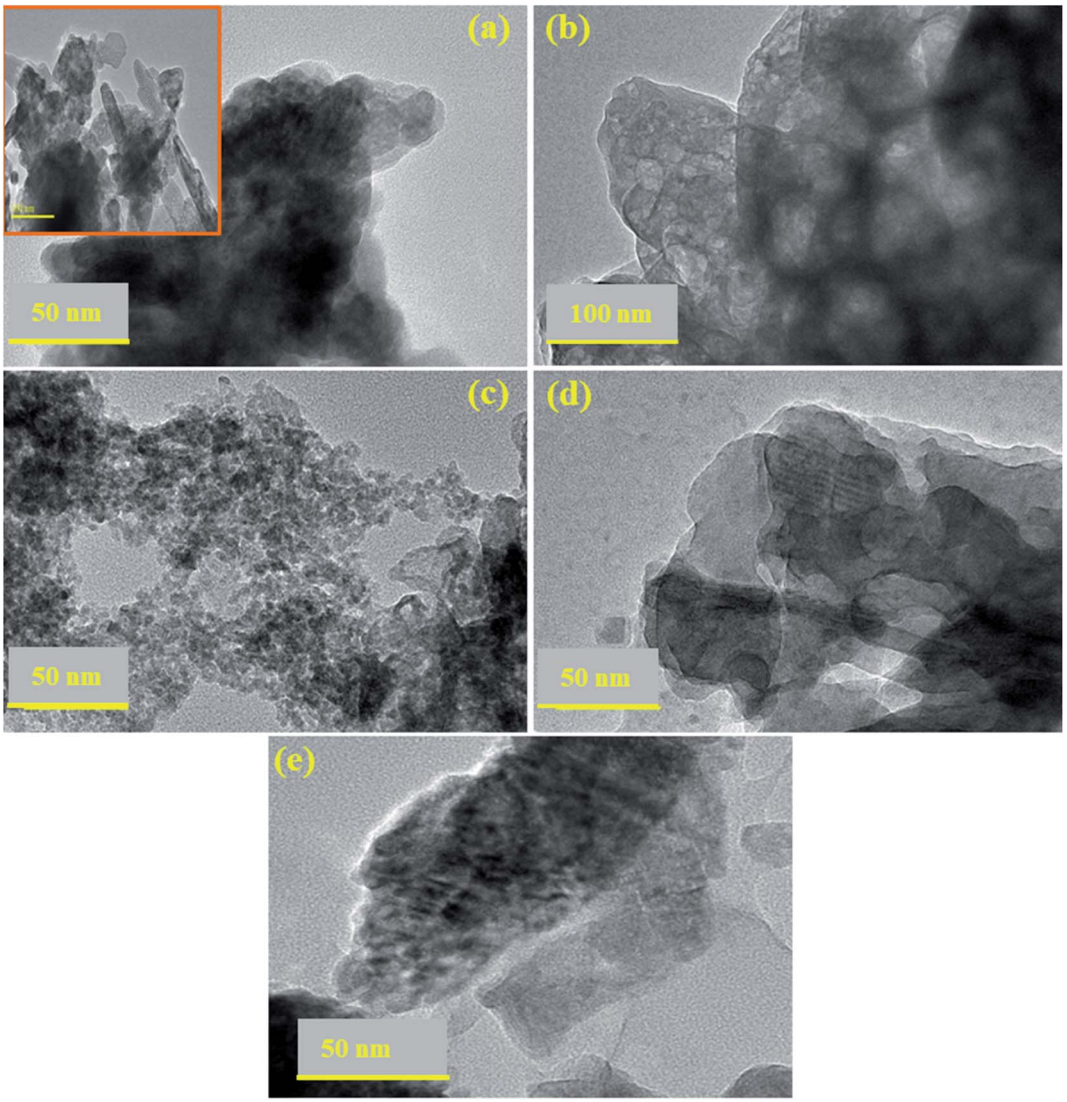

Fig. 6 TEM images (a–e) of ZnO and co-doped ZnO NRs; HR-TEM scale bar: 100 nm.

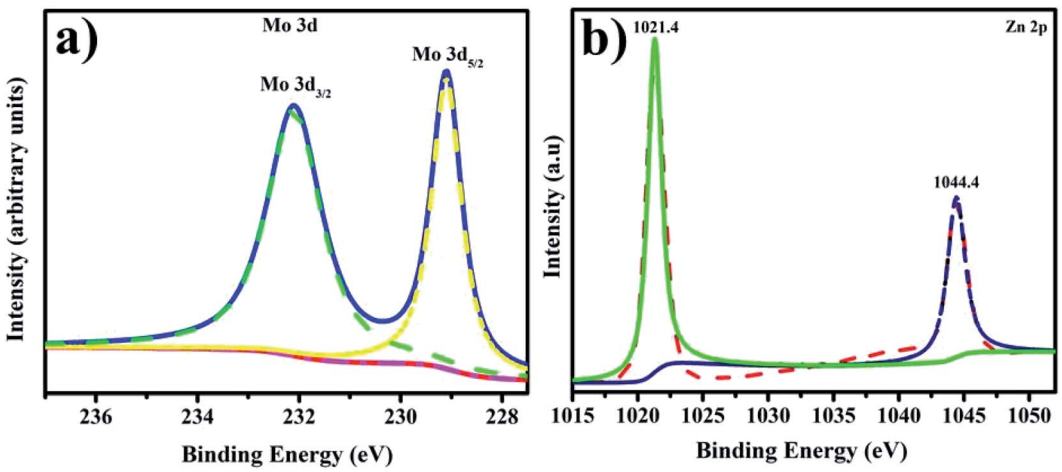

Fig. 7 (a and b) XPS spectra of the prepared NRs: (a) Mo 3d and (b) Zn 2p.

© 2022 The Author(s). Published by the Royal Society of Chemistry

Open Access Article. Published on 01 November 2021. Downloaded on 4/23/2026 6:19:45 PM.
This article is licensed under a Creative Commons Attribution-NonCommercial 3.0 Unported Licence.

Table 1 Antibacterial efficacy of ZnO, CNC and MoS_2-CNC-doped ZnO NRs

	Inhibition zone[a] (mm)		Inhibition zone[b] (mm)	
Sample	0.5 mg/50 μL	1.0 mg/50 μL	0.5 mg/50 μL	1.0 mg/50 μL
ZnO	3.35	4.30	0.95	1.25
CNC	3.30	4.45	0.95	1.65
CNC:ZnO	3.75	4.55	4.75	8.90
ZCM1	4.80	5.40	5.45	11.85
ZCM2	6.30	6.5	8.65	12.55
Ciprofloxacin	7.15	7.15	11.65	11.65
DIW	0	0	0	0

[a] Measurements of inhibition areas against G –ve. [b] Inhibition areas (mm) for G +ve.

shown in Table 1. The results showed that the synergistic effect was directly proportional to the NP concentration and inhibition zones (mm). Statistically significant ($p < 0.05$) inhibition zones for ZnO, CNC, CNC/ZnO, ZCM1 and ZCM2 were recorded as (3.35–6.30 nm) and (4.30–6.5 nm) for *E. coli* and (0.95–8.65 nm) and (1.25–12.55 nm) for *S. aureus* at low and high concentrations, respectively. Positive control ciprofloxacin showed 7.15 mm and 11.65 mm inhabitation zones towards *E. coli* and *S.* aureus in contrast to DI water (0 nm), respectively. Overall ZCM2 revealed significant anti-bacterial activity for G +ve relative to G –ve at both concentrations. The variation in oxidative stress is influenced by different variables such as the particle size, morphology and surface to mass ratios. Small sized particles contain reactive oxygen species (ROS), which encircle the bacterial cell membrane and cause bacterial death by the inhibition of the folate biosynthesis pathway enzymes DHFR and DHPS (Fig. 8 and 9).[24]

The role of *in silico* molecular docking in solving mysteries behind various biological activities is well documented. Enzymes belonging to the folate biosynthetic pathway have been reported as attractive targets for antibiotic discovery, for instance DHFR and DHPS (*i.e.* trimethoprim antibiotic).[51,52] Previously, Arularasu *et al.* reported cellulose/TiO_2 nanocomposites as anti-bacterial agents and identified possible interaction patterns with active site residues.[26] Here, we attempted to unveil the interactions of nanocomposites inside the active pocket of DHFR and DHPS enzymes from *E. coli* and *S. aureus*, which suggest these nanocomposites as possible inhibitors of these enzymes.

In the case of ZnO-CNC nanocomposites against the active site of $DHFR_{E.\ coli}$, the best docked conformation (binding score -9.671 kcal mol^{-1}) showed a H-bond with Asp27 (2.7 Å), Ile94 (2.1, 2.4 Å) and ALA (1.8 Å), where interacting residues are represented as sticks in Fig. 10(a), while the best binding score observed for ZnO-CNC-MoS_2 was -7.883 kcal mol^{-1} revealing H-bond interaction with Ile94 along with Pi–sulfur interaction with Phe31 as depicted in Fig. 10(b). The docked complexes with both nanocomposites with $DHFR_{E.\ coli}$ are depicted in Fig. 10(c) as superimposed structures showed their residence inside the pocket.

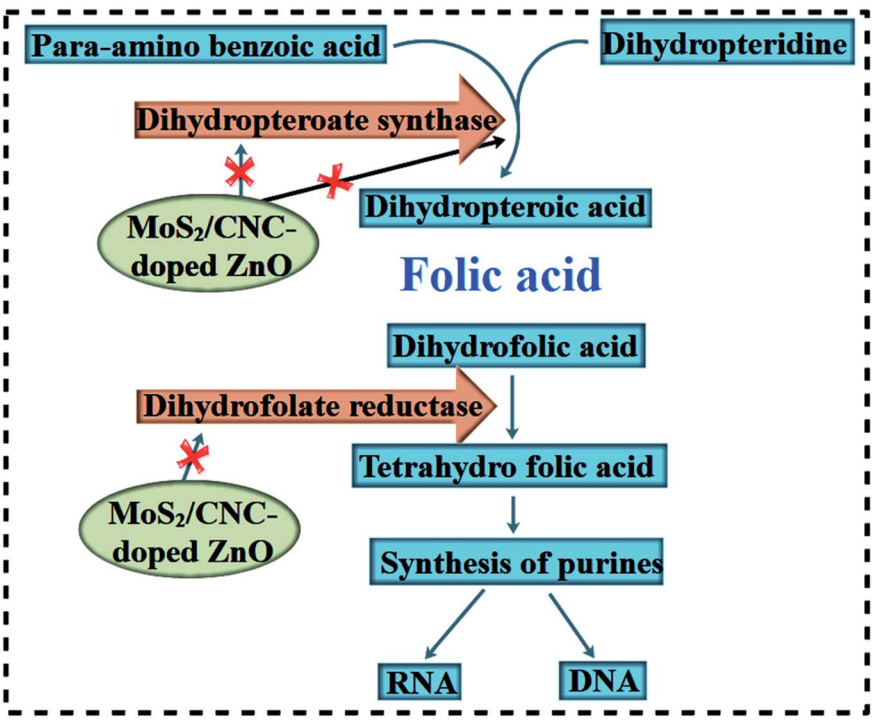

Fig. 8 Schematic illustration of the proposed antimicrobial mechanism of MoS_2@CNC/ZnO NRs as *in silico* molecular docking studies revealed the NR inhibitors of the folate biosynthesis pathway.

Open Access Article. Published on 01 November 2021. Downloaded on 4/23/2026 6:19:45 PM.
This article is licensed under a Creative Commons Attribution-NonCommercial 3.0 Unported Licence.

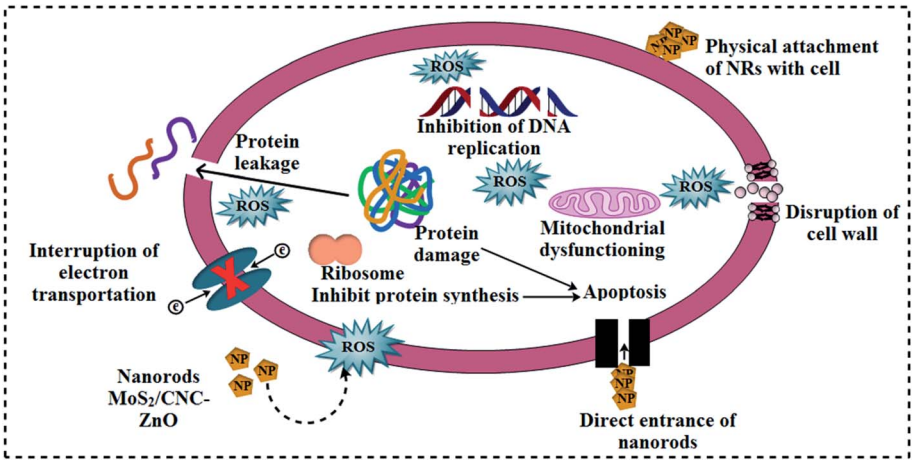

Fig. 9 Schematic illustration of the antimicrobial mechanism of MoS_2@CNC/ZnO NRs.

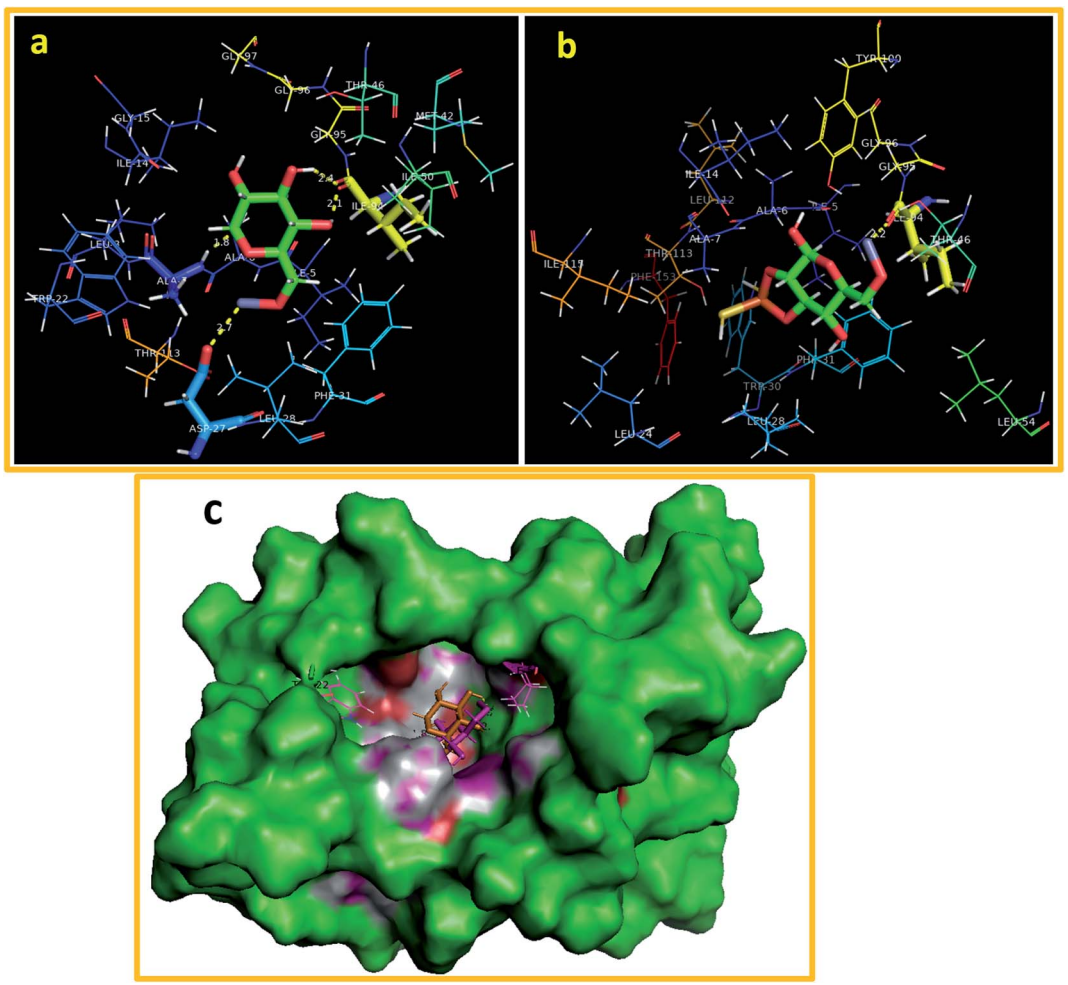

Fig. 10 Binding interaction pattern inside the active pocket of DHFR from *E. coli* (a) ZnO-CNC NPs and (b) ZnO-CNC-MoS_2 NPs and (c) 3D-structure representation of ZnO-CNC and ZnO-CNC-MoS_2-DHFR complexes (superimposed).

© 2022 The Author(s). Published by the Royal Society of Chemistry

Open Access Article. Published on 01 November 2021. Downloaded on 4/23/2026 6:19:45 PM.
This article is licensed under a Creative Commons Attribution-NonCommercial 3.0 Unported Licence.

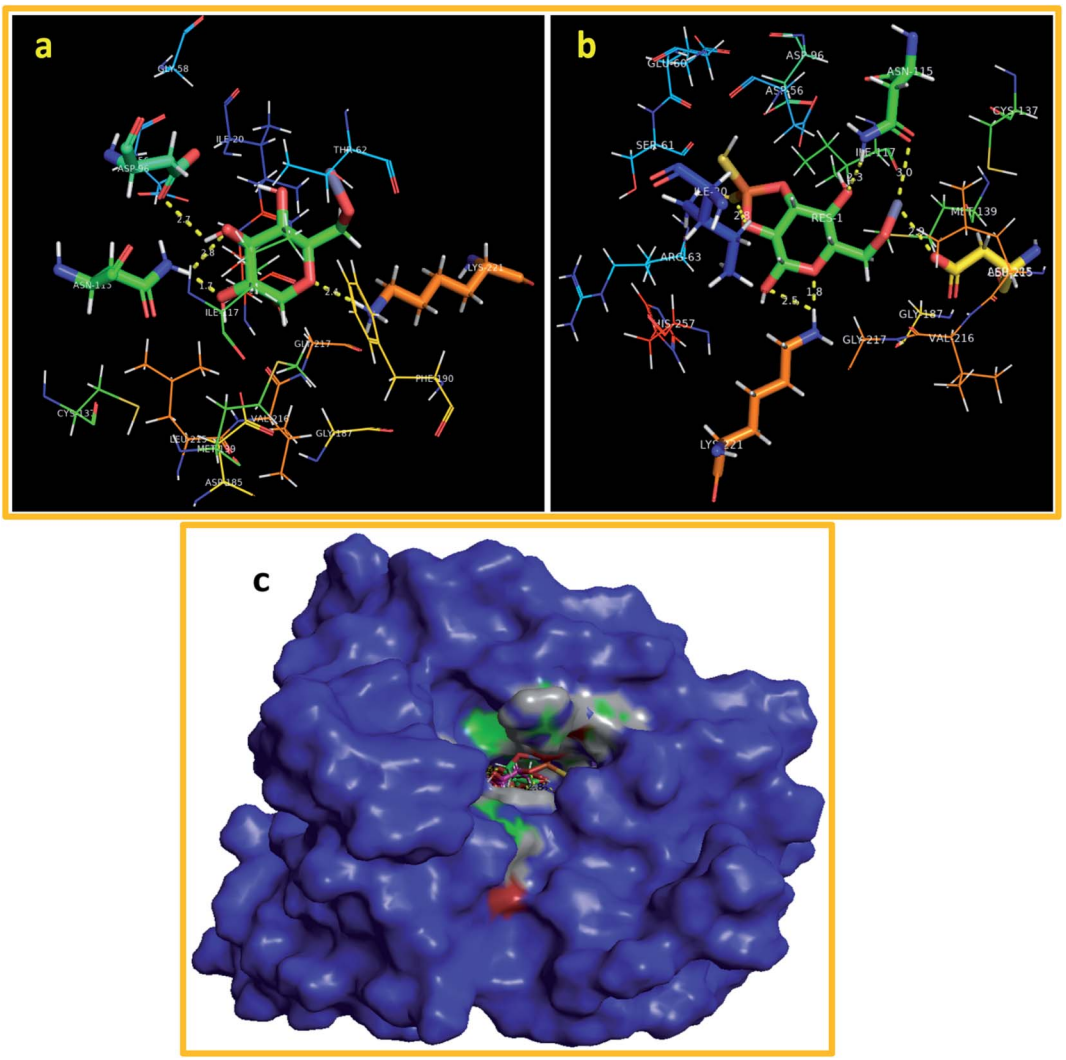

Fig. 11 Binding interaction pattern inside the active pocket of DHPS from *E. coli* (a) ZnO-CNC NPs and (b) ZnO-CNC-MoS_2 NPs and (c) 3D-structure representation of ZnO-CNC and ZnO-CNC-MoS_2-DHPS complexes (superimposed).

The best docked complex of ZnO-CNC against $DHPS_{E.\ coli}$ revealed H-bonding interaction with three amino acid residues of the active pocket *i.e.* Lys221 (2.1 Å), Asn115 (1.7 and 2.8 Å) and Asp96 (2.7 Å) with an overall binding score of −10.152 kcal mol^{-1} (Fig. 11(a)). Similarly, ZnO-CNC-MoS_2 showed a binding score of −9.773 kcal mol^{-1} having H-bond involvement with Asn115 (2.3 and 3.0 Å), Asp185 (2.9 Å), and Lys221 (1.8 and 2.5 Å) as shown in Fig. 11(b), while superimposed complexes are depicted in Fig. 11(c).

Furthermore, the docking predictions of ZnO-CNC NPs against the active pocket of DHFR *S. aureus* also revealed a good binding tendency (binding score: −6.779 kcal mol^{-1}) and interaction pattern, representing the involvement of Asp27 (H-bond: 2.5 Å) and ALA7 (H-bond: 1.8 and 2.8 Å). A similar trend was observed for ZnO-CNC-MoS_2 (binding score: −5.639 kcal mol^{-1}) showing interaction with ALA7 (1.7 and 2.7 Å) and Asp27 (2.7 Å) through H-bonds as depicted in Fig. 12(a) and b, while superimposed complexes for both nanocomposites are shown in Fig. 12(c).

To check the catalytic performance of ZnO, CNC, ZnO-CNC and MoS_2/CNC-doped ZnO NRs, UV-vis spectra were attained using methylene blue (Mb) dye as the contaminant to be degraded in the presence of each sample. Pure and MoS_2/CNC-doped ZnO NRs showed a maximum dye degradation of 10.2, 67.6, 69.36 and 69.44% in an acidic medium (pH = 4) and 30.2, 8.29, 32.4, 35.08 and 44.55 in a neutral medium (pH = 7), respectively, as expressed in Fig. 13(a and b). The maximum catalytic performance was observed in acidic solution with higher doping of MoS_2/CNC into ZnO NRs within 15 minutes. Catalytic activity was influenced by the surface area, morphology and crystallinity of the nanoparticles. In the present work, the consequent improvement perceived in the catalytic performance is ascribed to a change in the morphology (nanorods) (Table 2).

© 2022 The Author(s). Published by the Royal Society of Chemistry

Open Access Article. Published on 01 November 2021. Downloaded on 4/23/2026 6:19:45 PM.
This article is licensed under a Creative Commons Attribution-NonCommercial 3.0 Unported Licence.

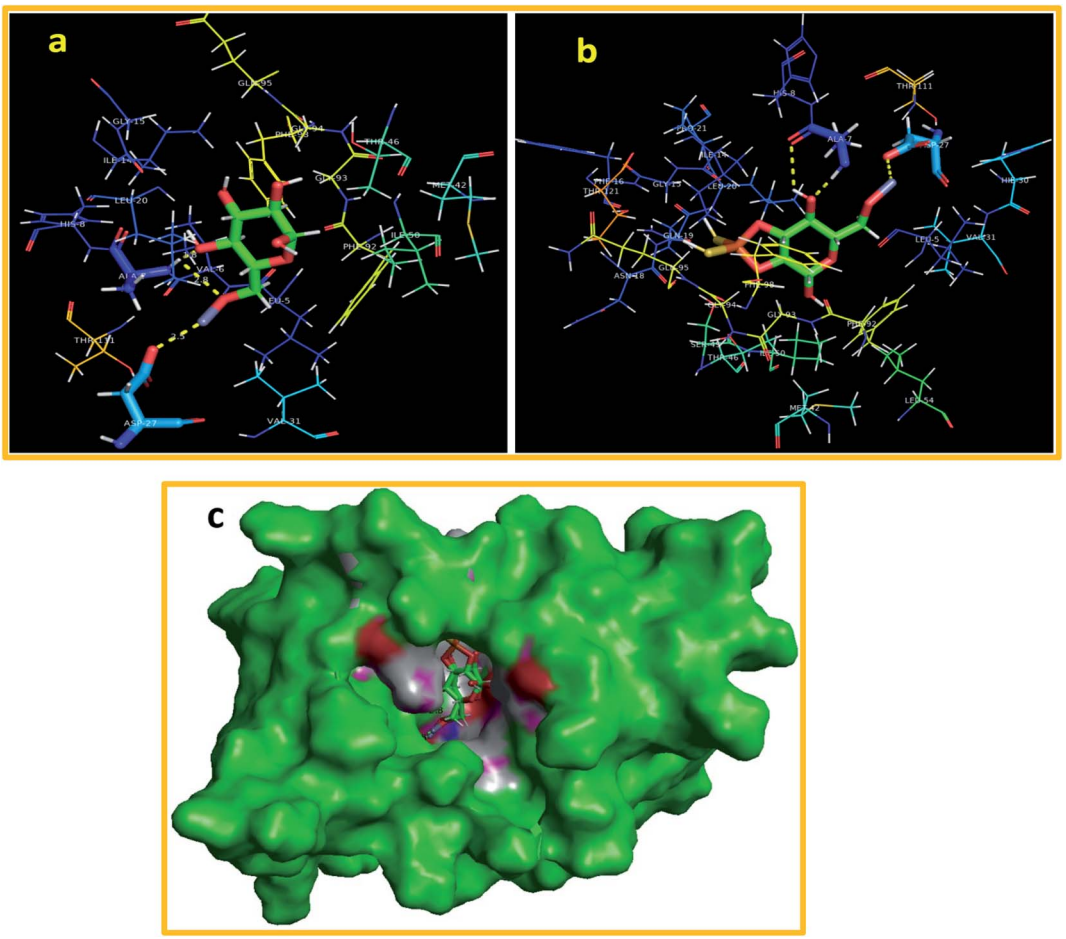

Fig. 12 Binding interaction pattern inside the active pocket of DHPS from *S. aureus* (a) ZnO-CNC NPs and (b) ZnO-CNC-MoS_2 NPs and (c) 3D-structure representation of ZnO-CNC and ZnO-CNC-MoS_2-DHPS complexes (superimposed).

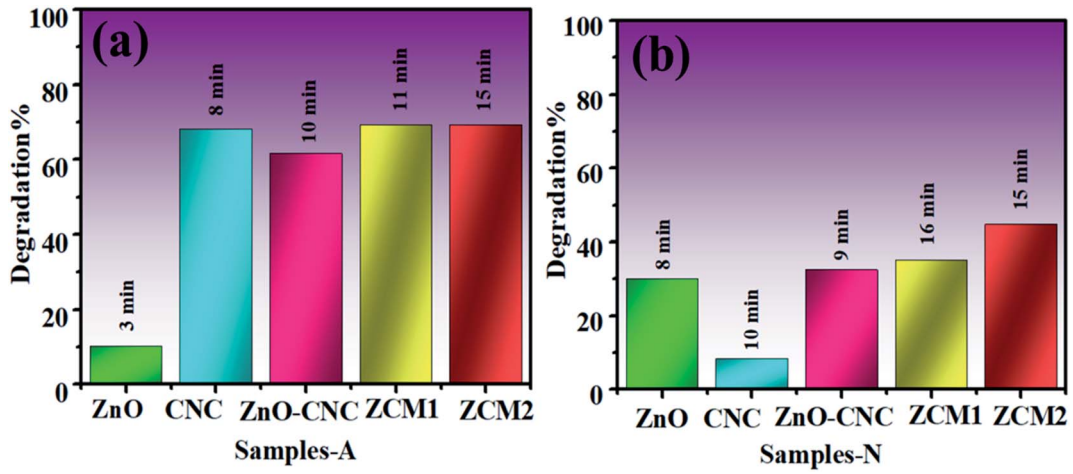

Fig. 13 Catalysis of ZnO, CNC, ZnO-CNC, ZCM1 and ZCM2 in (a) acidic and (b) neutral media.

© 2022 The Author(s). Published by the Royal Society of Chemistry

Open Access Article. Published on 01 November 2021. Downloaded on 4/23/2026 6:19:45 PM. This article is licensed under a Creative Commons Attribution-NonCommercial 3.0 Unported Licence.

Table 2 Comparison of results for the degradation of methylene blue: ciprofloxacin by $NaBH_4$ in the presence of catalysts

Catalyst	Dye	Reaction time	Catalyst amount	Degradation result	References
$CuO/TiO_2/ZnO$ NCs	Crystal violet	360 s	5 mg L^{-1}	82.18%	53
GO-doped MgO NSc	Methylene blue: ciprofloxacin	80 s	3 mg L^{-1}	45%	54
Cu/ZnO NCs	Malachite green and rhodamine B	180 s	10 mg L^{-1}	52%	55
CuO NPs/clinoptilolite	Methylene blue and rhodamine B	15 s	7 mg L^{-1}	60%	56
ZCM2 NRs	Methylene blue	15 min	3 mg L^{-1}	69.44%	Present study

4. Conclusion

In the current study, MoS_2/CNC-doped ZnO NRs were synthesized successfully to achieve an enhanced bactericidal effect and catalytic performance. According to experimental results, ZnO exhibited a hexagonal wurtzite phase and the crystalline size was found to be increased (26.2–48.5 nm) upon co-doping, while the presence of Mo–S vibration and the formation of ZnO NRs were confirmed by FTIR and EDS. The rod-like morphology, *d*-spacing and agglomeration upon CNC and MoS_2 doping in ZnO NRs were confirmed by HR-TEM. UV spectra revealed a blueshift due to the doping of MoS_2/CNC, causing the band gap to narrow in comparison to the undoped (3.3–2.3 eV). When MoS_2/CNC was doped into ZnO, the PL intensity decreased, resulting in a reduced electron–hole pair recombination rate. The dye degradation effectiveness of NRs against MB dye was determined in acidic and neutral media. A maximum degradation of 68.44% was observed for ZCM2. Overall the experimental outcomes revealed MoS_2@ZnO/CNC-0.2 (ZCM2) as a significant bactericidal agent for G +ve relative to G −ve at both concentrations. *In silico* molecular docking investigations suggested ZnO-CNC and ZnO-CNC-MoS_2 nanocomposites as possible inhibitors of DHFR and DHPS enzymes of the folate biosynthetic pathway. According to the results of this study, the synthesised ZnO and MoS_2/CNC-doped NRs have demonstrated excellent antibacterial and catalytic effectiveness for the treatment of industrially contaminated wastewater and for usage in biomedical applications.

Availability of data and materials

All data are fully available on demand.

Funding

The authors are thankful to HEC for financial support through start research grant project # 21-1669/SRGP/R&D/HEC/2017 Pakistan.

Conflicts of interest

The authors confirm that this manuscript has no conflict of interest.

Acknowledgements

Support provided by the Core Research Facilities at the King Fahd University of Petroleum & Minerals, Dhahran, Saudi Arabia is greatly appreciated.

References

1 S. Kumar, V. Maivizhikannan, J. Drews and V. Krishnan, Fabrication of nanoheterostructures of boron doped ZnO-MoS_2 with enhanced photostability and photocatalytic activity for environmental remediation applications, *Vacuum*, 2019, **163**, 88–98, DOI: 10.1016/j.vacuum.2019.02.001.

2 S. Kumar, A. Kumar, A. Bahuguna, V. Sharma and V. Krishnan, Two-dimensional carbon-based nanocomposites for photocatalytic energy generation and environmental remediation applications, *J. Nanotechnol.*, 2017, 1571–1600, DOI: 10.3762/bjnano.8.159.

3 R. Sankaranarayanan, Worldwide burden of gynaecological cancer : The size of the problem, *Best Pract. Res.*, 2006, **20**, 207–225, DOI: 10.1016/j.bpobgyn.2005.10.007.

4 H. Li, H. Shen, L. Duan, R. Liu, Q. Li, Q. Zhang and X. Zhao, Enhanced photocatalytic activity and synthesis of ZnO nanorods/MoS_2 composites, *Superlattices Microstruct.*, 2018, **117**, 336–341, DOI: 10.1016/j.spmi.2018.03.028.

5 K. J. Chen, T. H. Fang, F. Y. Hung, L. W. Ji, S. J. Chang, S. J. Young and Y. J. Hsiao, The crystallization and physical properties of Al-doped ZnO nanoparticles, *Appl. Surf. Sci.*, 2008, **254**, 5791–5795, DOI: 10.1016/j.apsusc.2008.03.080.

6 S. Sadri Moghaddam, M. R. Alavi Moghaddam and M. Arami, Coagulation/flocculation process for dye removal using sludge from water treatment plant: Optimization through response surface methodology, *J. Hazard. Mater.*, 2010, **175**, 651–657, DOI: 10.1016/j.jhazmat.2009.10.058.

7 L. Zhu, L. Zong, X. Wu, M. Li, H. Wang, J. You and C. Li, Shapeable Fibrous Aerogels of Metal-Organic-Frameworks Templated with Nanocellulose for Rapid and Large-Capacity Adsorption, *ACS Nano*, 2018, **12**, 4462–4468, DOI: 10.1021/acsnano.8b00566.

8 K. Alamelu, V. Raja, L. Shiamala and B. M. Jaffar Ali, Biphasic TiO 2 nanoparticles decorated graphene nanosheets for visible light driven photocatalytic degradation of organic dyes, *Appl. Surf. Sci.*, 2018, **430**, 145–154, DOI: 10.1016/j.apsusc.2017.05.054.

9 E. M. Siedlecka, A. Ofiarska, A. F. Borzyszkowska, A. Białk-Bielińska, P. Stepnowski and A. Pieczyńska, Cytostatic drug

Open Access Article. Published on 01 November 2021. Downloaded on 4/23/2026 6:19:45 PM. This article is licensed under a Creative Commons Attribution-NonCommercial 3.0 Unported Licence.

removal using electrochemical oxidation with BDD electrode: Degradation pathway and toxicity, *Water Res.*, 2018, **144**, 235–245, DOI: 10.1016/j.watres.2018.07.035.

10 S. Rajoriya, S. Bargole, S. George and V. K. Saharan, Treatment of textile dyeing industry effluent using hydrodynamic cavitation in combination with advanced oxidation reagents, *J. Hazard. Mater.*, 2018, **344**, 1109–1115, DOI: 10.1016/j.jhazmat.2017.12.005.

11 H. Li, L. Zhang, H. Lu, J. Ma, X. Zhou, Z. Wang and C. Yi, Macro-/nanoporous Al-doped ZnO/cellulose composites based on tunable cellulose fiber sizes for enhancing photocatalytic properties, *Carbohydr. Polym.*, 2020, **250**, 116873, DOI: 10.1016/j.carbpol.2020.116873.

12 S. A. Ansari, M. M. Khan, M. O. Ansari, J. Lee and M. H. Cho, Biogenic Synthesis, Photocatalytic, and Photoelectrochemical Performance of Ag–ZnO Nanocomposite, *Phys. Chem.*, 2013, **117**, 27023–27030.

13 G. P. Awasthi, S. P. Adhikari, S. Ko, H. J. Kim, C. H. Park and C. S. Kim, Facile synthesis of ZnO flowers modified graphene like MoS_2 sheets for enhanced visible-light-driven photocatalytic activity and antibacterial properties, *J. Alloys Compd.*, 2016, **682**, 208–215, DOI: 10.1016/j.jallcom.2016.04.267.

14 I. Poulios, E. Micropoulou, R. Panou and E. Kostopoulou, Photooxidation of eosin Y in the presence of semiconducting oxides, *Appl. Catal., B*, 2003, **41**, 345–355, DOI: 10.1016/S0926-3373(02)00160-1.

15 A. Khataee, R. D. C. Soltani, Y. Hanifehpour, M. Safarpour, H. Gholipour Ranjbar and S. W. Joo, Synthesis and characterization of dysprosium-doped ZnO nanoparticles for photocatalysis of a textile dye under visible light irradiation, *Ind. Eng. Chem. Res.*, 2014, **53**, 1924–1932, DOI: 10.1021/ie402743u.

16 S. P. Adhikari, H. R. Pant, J. H. Kim, H. J. Kim, C. H. Park and C. S. Kim, One pot synthesis and characterization of Ag-ZnO/g-C_3N_4 photocatalyst with improved photoactivity and antibacterial properties, *Colloids Surf., A*, 2015, **482**, 477–484, DOI: 10.1016/j.colsurfa.2015.07.003.

17 Y. H. Tan, K. Yu, J. Z. Li, H. Fu and Z. Q. Zhu, MoS_2@ZnO nano-heterojunctions with enhanced photocatalysis and field emission properties, *J. Appl. Phys.*, 2014, **116**, 064305, DOI: 10.1063/1.4893020.

18 J. Ma, Z. Sun, Z. Wang and X. Zhou, Preparation of ZnO–cellulose nanocomposites by different cellulose solution systems with a colloid mill, *Cellulose*, 2016, **23**, 3703–3715, DOI: 10.1007/s10570-016-1081-0.

19 A. Farooq, M. K. Patoary, M. Zhang, H. Mussana, M. Li, M. A. Naeem, M. Mushtaq, A. Farooq and L. Liu, Cellulose from sources to nanocellulose and an overview of synthesis and properties of nanocellulose/zinc oxide nanocomposite materials, *Int. J. Biol. Macromol.*, 2020, **154**, 1050–1073, DOI: 10.1016/j.ijbiomac.2020.03.163.

20 M. Ikram, S. Hayat, M. Imran, A. Haider, S. Naz, A. Ul-Hamid, I. Shahzadi, J. Haider, A. Shahzadi, W. Nabgan and S. Ali, Novel Ag/cellulose-doped CeO_2 quantum dots for efficient dye degradation and bactericidal activity with molecular docking study, *Carbohydr. Polym.*, 2021, **269**, 118346, DOI: 10.1016/j.carbpol.2021.118346.

21 K. N. Mohd Amin, P. K. Annamalai, I. C. Morrow and D. Martin, Production of cellulose nanocrystals *via* a scalable mechanical method, *RSC Adv.*, 2015, **5**, 57133–57140, DOI: 10.1039/c5ra06862b.

22 G. Vijayaprasath, R. Murugan, Y. Hayakawa and G. Ravi, Optical and magnetic studies on Gd doped ZnO nanoparticles synthesized by co-precipitation method, *J. Lumin.*, 2016, **178**, 375–383, DOI: 10.1016/j.jlumin.2016.06.004.

23 A. H. M. Ijaz, M. I. M. Naz, H. M. J. A. Khan and M. M. A. M. Ikram, Enhanced bactericidal action and dye degradation of spicy roots ' extract - incorporated fine - tuned metal oxide nanoparticles, *Appl. Nanosci.*, 2020, **10**, 1095–1104, DOI: 10.1007/s13204-019-01188-x.

24 M. Ikram, I. Hussain, J. Hassan, A. Haider, M. Imran, M. Aqeel and S. Ali, Evaluation of antibacterial and catalytic potential of copper-doped chemically exfoliated boron nitride nanosheets, *Ceram. Int.*, 2020, **46**, 21073–21083, DOI: 10.1016/j.ceramint.2020.05.180.

25 S. A. U. Qumar, M. Ikram, M. Imran, A. Haider, A. Ul-Hamid, J. Haider and K. N. Riaz, Synergetic effect of Bi-doped exfoliated MoS_2 nanosheets on its bactericidal and dye degradation potential, *Dalton Trans.*, 2020, **49**, 5362, DOI: 10.1039/d0dt00924e.

26 M. V Arularasu, M. Harb and R. Sundaram, Synthesis and characterization of cellulose/TiO 2 nanocomposite : Evaluation of *in vitro* antibacterial and *in silico* molecular docking studies, *Carbohydr. Polym.*, 2020, **249**, 116868, DOI: 10.1016/j.carbpol.2020.116868.

27 R. L. Summerfield, D. M. Daigle, S. Mayer, D. Mallik, D. W. Hughes, S. G. Jackson, M. Sulek, M. G. Organ, E. D. Brown and M. S. Junop, A 2. 13 ÅStructure of E. coli Dihydrofolate Reductase Bound to a Novel Competitive Inhibitor Reveals a New Binding Surface Involving the M20 Loop Region, *J. Med. Chem.*, 2006, **49**, 6977–6986.

28 M. L. Dennis, M. D. Lee, J. R. Harjani, M. Ahmed, A. J. DeBono, N. P. Pitcher, Z. C. Wang, S. Chhabra, N. Barlow, R. Rahmani, B. Cleary, O. Dolezal, M. Hattarki, L. Aurelio, J. Shonberg, B. Graham, T. S. Peat, J. B. Baell and J. D. Swarbrick, 8-Mercaptoguanine Derivatives as Inhibitors of Dihydropteroate Synthase, *Chem.–Eur. J.*, 2018, **24**, 1922–1930, DOI: 10.1002/chem.201704730.

29 B. Nammalwar, C. R. Bourne, R. A. Bunce, N. Wakeham, P. C. Bourne, K. Ramnarayan, S. Mylvaganam, K. D. Berlin, E. W. Barrow and W. W. Barrow, Inhibition of Bacterial Dihydrofolate Reductase by 6-Alkyl-2,4-diaminopyrimidines, *ChemMedChem*, 2012, **7**, 1974–1982, DOI: 10.1002/cmdc.201200291.

30 M. S. Sharif, M. Aqeel, A. Haider, S. Naz, M. Ikram, A. Ul-Hamid, J. Haider, I. Aslam, A. Nazir and A. R. Butt, Photocatalytic, Bactericidal and Molecular Docking Analysis of Annealed Tin Oxide Nanostructures, *Nanoscale Res. Lett.*, 2021, **16**, 1–16, DOI: 10.1186/s11671-021-03495-1.

31 S. Altaf, A. Haider, S. Naz, A. Ul-Hamid, J. Haider, M. Imran, A. Shahzadi, M. Naz, H. Ajaz and M. Ikram, Comparative Study of Selenides and Tellurides of Transition Metals (Nb and Ta) with Respect to its Catalytic, Antimicrobial, and

 © 2022 The Author(s). Published by the Royal Society of Chemistry

Open Access Article. Published on 01 November 2021. Downloaded on 4/23/2026 6:19:45 PM.
This article is licensed under a Creative Commons Attribution-NonCommercial 3.0 Unported Licence.

Molecular Docking Performance, *Nanoscale Res. Lett.*, 2020, **15**, 144, DOI: 10.1186/s11671-020-03375-0.

32 M. T. R. Abagyan, Biased Probability Monte Carlo Conformational Searches and Electrostatic Calculations for Peptides and Proteins, *J. Mol. Biol.*, 1994, 983–1002.

33 N. Tian, Z. Li, D. Xu, Y. Li, W. Peng, G. Zhang, F. Zhang and X. Fan, Utilization of MoS_2 Nanosheets to Enhance the Photocatalytic Activity of ZnO for the Aerobic Oxidation of Benzyl Halides under Visible Light, *Ind. Eng. Chem. Res.*, 2016, **55**, 8726–8732, DOI: 10.1021/acs.iecr.6b01420.

34 M. V Arularasu, M. Harb and R. Sundaram, Synthesis and characterization of cellulose/TiO_2 nanocomposite: Evaluation of *in vitro* antibacterial and *in silico* molecular docking studies, *Carbohydr. Polym.*, 2020, **249**, 116868, DOI: 10.1016/j.carbpol.2020.116868.

35 M. Ikram, S. Aslam, A. Haider, S. Naz, A. Ul-Hamid, A. Shahzadi, M. Ikram, J. Haider, S. O. A. Ahmad and A. R. Butt, Doping of Mg on ZnO Nanorods Demonstrated Improved Photocatalytic Degradation and Antimicrobial Potential with Molecular Docking Analysis, *Nanoscale Res. Lett.*, 2021, **16**, DOI: 10.1186/s11671-021-03537-8.

36 Y. Wu, J. Yun, L. Wang and X. Yang, Structure and optical properties of Mg-doped ZnO nanoparticles by polyacrylamide method, *Cryst. Res. Technol.*, 2013, **48**, 145–152, DOI: 10.1002/crat.201200438.

37 K. Lefatshe, C. M. Muiva and L. P. Kebaabetswe, Extraction of nanocellulose and in-situ casting of ZnO/cellulose nanocomposite with enhanced photocatalytic and antibacterial activity, *Carbohydr. Polym.*, 2017, **164**, 301–308, DOI: 10.1016/j.carbpol.2017.02.020.

38 X. Song, Y. Liu, Y. Zheng, K. Ding, S. Nie and P. Yang, Synthesis of butterfly-like ZnO nanostructures and study of their self-reducing ability toward Au3+ ions for enhanced photocatalytic efficiency, *Phys. Chem. Chem. Phys.*, 2016, **18**, 4577–4584, DOI: 10.1039/c5cp07187a.

39 Y. W. Chen, H. V. Lee and S. B. A. Hamid, Preparation of nanostructured cellulose *via* Cr(III)- and Mn(II)-transition metal salt catalyzed acid hydrolysis approach, *BioResources*, 2016, **11**, 7224–7241, DOI: 10.15376/biores.11.3.7224-7241.

40 R. N. Ali, H. Naz, J. Li, X. Zhu, P. Liu and B. Xiang, Band gap engineering of transition metal (Ni/Co) codoped in zinc oxide (ZnO) nanoparticles, *J. Alloys Compd.*, 2018, **744**, 90–95, DOI: 10.1016/j.jallcom.2018.02.072.

41 S. Ghosh, M. Saha and S. K. De, Tunable surface plasmon resonance and enhanced electrical conductivity of in doped ZnO colloidal nanocrystals, *Nanoscale*, 2014, **6**, 7039–7051, DOI: 10.1039/c3nr05608b.

42 B. Ghanbari Shohany and A. Khorsand Zak, Doped ZnO nanostructures with selected elements - Structural, morphology and optical properties: A review, *Ceram. Int.*, 2020, **46**, 5507–5520, DOI: 10.1016/j.ceramint.2019.11.051.

43 C. Shi, L. Zhang, H. Bian, Z. Shi, J. Ma and Z. Wang, *Construction of Ag–ZnO/cellulose Nanocomposites via Tunable Cellulose Size for Improving Photocatalytic Performance*, Elsevier Ltd, 2021. DOI: DOI: 10.1016/j.jclepro.2020.125089.

44 A. K. Pradhan, K. Zhang, G. B. Loutts, U. N. Roy, Y. Cui and A. Burger, Structural and spectroscopic characteristics of ZnO and ZnO: Er 3+ nanostructures, *J. Phys. Condens. Matter.*, 2004, **16**, 7123–7129, DOI: 10.1088/0953-8984/16/39/043.

45 Z. Y. Xue, D. H. Zhang, Q. P. Wang and J. H. Wang, The blue photoluminescence emitted from ZnO films deposited on glass substrate by rf magnetron sputtering, *Appl. Surf. Sci.*, 2002, **195**, 126–129, DOI: 10.1016/S0169-4332(02)00547-0.

46 S. G. Nedilko, S. L. Revo, V. P. Chornii, V. P. Scherbatskyi and M. S. Nedielko, Luminescent determination of nitrite traces in water solutions using cellulose as sorbent, *J. Sensors Sens. Syst.*, 2015, **4**, 31–36, DOI: 10.5194/jsss-4-31-2015.

47 M. B. Tahir, M. Sohaib, M. Rafique, M. Sagir, N. U. Rehman and S. Muhammad, Visible light responsive photocatalytic hydrogen evolution using MoS_2 incorporated ZnO, *Appl. Nanosci.*, 2020, **10**, 3925–3931, DOI: 10.1007/s13204-020-01476-x.

48 M. V. Shankar and V. Krishnan, Defect-Rich MoS_2 Ultrathin Nanosheets-Coated Nitrogen-Doped ZnO Nanorod Heterostructures: An Insight into in-Situ-Generated ZnS for Enhanced Photocatalytic Hydrogen Evolution, *ACS Appl. Energy Mater.*, 2019, **2**(8), 5622–5634, DOI: 10.1021/acsaem.9b00790.

49 W. Ji, R. Shen, R. Yang, G. Yu, X. Guo, L. Peng and W. Ding, Partially nitrided molybdenum trioxide with promoted performance as an anode material for lithium-ion batteries, *J. Mater. Chem. A*, 2014, **2**, 699–704, DOI: 10.1039/c3ta13708b.

50 B. Fan, Q. Yao, C. Wang, Y. Xiong, Q. Sun and C. Jin, Spawns Structure of Rod-Like ZnO Wrapped in Cellulose Nanofibers for Electromagnetic Wave Absorption, *J. Nanomater.*, 2017, **2017**, 6, DOI: 10.1155/2017/6329072.

51 G. E. Dale, C. Broger, A. D'Arcy, P. G. Hartman, R. DeHoogt, S. Jolidon, I. Kompis, A. M. Labhardt, H. Langen, H. Locher, M. G. P. Page, D. Stüber, R. L. Then, B. Wipf and C. Oefner, A single amino acid substitution in Staphylococcus aureus dihydrofolate reductase determines trimethoprim resistance, *J. Mol. Biol.*, 1997, **266**, 23–30, DOI: 10.1006/jmbi.1996.0770.

52 G. H. Hitchings, Mechanism of Action of Trimethoprim-Sulfamethoxazole-I, *J. Infect. Dis.*, 1973, **128**, S433–S436.

53 C. Mathalai Sundaram, S. Kalpana, S. Rafi Ahamed, V. Sivaganesan and E. Nandhakumar, Studies on the catalytic activity of CuO/TiO2/ZnO ternary nanocomposites prepared *via* one step hydrothermal green approach, *Mater. Res. Express*, 2019, **6**, 125043, DOI: 10.1088/2053-1591/ab57d9.

54 M. Ikram, T. Inayat, A. Haider, A. U. Hamid, J. Haider, W. Nabgan, A. Saeed, A. Shahbaz and S. Hayat, Graphene Oxide - Doped MgO Nanostructures for Highly Efficient Dye Degradation and Bactericidal Action, *Nanoscale Res. Lett.*, 2021, **16**, 56, DOI: 10.1186/s11671-021-03516-z.

55 A. Sankaran and K. Kumaraguru, The novel two step synthesis of CuO/ZnO and CuO/CdO nanocatalysts for enhancement of catalytic activity, *J. Mol. Struct.*, 2020, **1221**, 128772, DOI: 10.1016/j.molstruc.2020.128772.

56 M. Bordbar and Z. Shari, Green synthesis of copper oxide nanoparticles/clinoptilolite using *Rheum palmatum* L. root extract : high catalytic activity for reduction of 4-nitro phenol, rhodamine B, and methylene blue, *J. Sol-Gel Sci. Technol.*, 2017, **81**, 724–733, DOI: 10.1007/s10971-016-4239-1.